Journal of Colloid and Interface Science 461 (2016) 162–167

Contents lists available at ScienceDirect

Journal of Colloid and Interface Science

journal homepage: www.elsevier.com/locate/jcis

Short Communication

Synthesis of tunable-band-gap "Open-Box" halide perovskites by use of anion exchange and internal dissolution procedures

Zhengcui Wu [a,b,1], Baohua Wang [a,1], Jian He [a], Tao Chen [a,*]

[a] Department of Physics, The Chinese University of Hong Kong, Shatin, N.T., Hong Kong, China
[b] Anhui Key Laboratory of Molecule-Based Materials, The Key Laboratory of Functional Molecular Solids, Ministry of Education, College of Chemistry and Materials Science, Anhui Normal University, Wuhu 241000, PR China

GRAPHICAL ABSTRACT

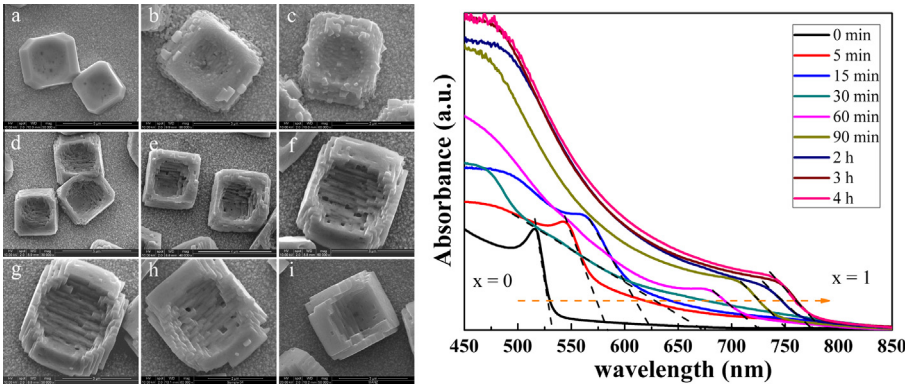

ARTICLE INFO

Article history:
Received 22 July 2015
Revised 1 September 2015
Accepted 1 September 2015
Available online 5 September 2015

Keywords:
Organolead halide perovskites
Kerkindall effect
Tunable band gap
Anion exchange

ABSTRACT

We demonstrate the synthesis of cuboid $MAPbBr_3$ ($MA = CH_3NH_3$) microcrystals and subsequent conversion into open-box-like $MAPb(Br_{1-x}I_x)_3$ ($0 \leqslant x \leqslant 1$) microcrystals by anion exchange in MAI solution. During the substitution of Br^- with I^-, the initial cuboid framework of $MAPbBr_3$ crystals is retained. The preferential internal dissolution of $MAPbBr_3$ due to the surface coverage and protection of $MAPb(Br_{1-x}I_x)_3$ induces voids inside the cuboid crystals, finally leading to open-box-like iodide-rich $MAPb(Br_{1-x}I_x)_3$. By controlling the degree of anion exchange, the intense light absorption of the product is able to be tuned in specific wavelengths throughout the visible range. This solution-phase anion exchange approach provides a synthetic strategy in designing sophisticated organolead halide perovskites structures as well as tuning the band gaps for further applications across a range of possible domains.

1. Introduction

Organolead perovskites $MAPbX_3$ ($MA = CH_3NH_3$, X = Cl, Br or I) show extraordinary promise in solar cells as light absorbing materials due to their solution-processability, easy crystallization, intense light absorption and long charge carrier diffusion length [1–8]. In general, three ways have been developed to prepare organolead halide perovskite, i.e. one-step spin-coating route [3,9–14], two-step sequential deposition approach [1,15–18], and thermal evaporation method through co-evaporation of lead halide and alkyl ammonium halide [2,19]. All of these preparation methods

* Corresponding author.
E-mail address: taochen@phy.cuhk.edu.hk (T. Chen).
[1] These authors contributed equally to this work.

http://dx.doi.org/10.1016/j.jcis.2015.09.005
0021-9797/

can generate high-quality perovskite film and have been well studied in order to boost the energy conversion efficiency.

Compared with the preparation of perovskite film for solar cells, little attention has been paid to the exploration of nanostructured perovskite. However, the initial investigations have found encouraging property of nanostructured perovskite for optoelectronic devices. For example, the organolead perovskite ($CH_3NH_3PbI_{3-a}X_a$, X = I, Br, Cl) nanoplates are able to serve as high quality planar room-temperature NIR nanolasers [20]. Single-crystal lead halide perovskite nanowires are found to possess room-temperature and wavelength-tunable lasing property [21]. The nanostructured $MAPbI_3$ film with micrometer grain size and high surface coverage enables photovoltaic devices with a power conversion efficiency of 10.6% [22]. A series of porous and anisotropic perovskite nanostructures have been synthesized and the nanowires have demonstrated the application as high-performance visible-light photodetectors [23,24].

Herein, we develop a convenient method for the synthesis of single-crystalline cuboid $MAPbBr_3$ microcrystals and show that the Br^- anion in the perovskite can be replaced by I^- anion, allowing finely tuning the halide composition and controlling the crystal structures and band gaps. During the reaction, the anion exchange and internal dissolution process induce open-box-like $MAPb(Br_{1-x}I_x)_3$ ($0 \leqslant x \leqslant 1$) crystals with controllable composition and band gap, providing further advancement of these functional materials.

2. Experimental section

2.1. Preparation of $MAPbBr_3$ perovskite solution

MABr powder was synthesized according to the literature with minor modifications [13]. Briefly, 50 mL of hydrobromic acid (48% in water) and 30 mL of methylamine (40% in methanol) were mixed together in a 250 mL round-bottom flask maintaining at 0 °C for 2 h with stirring throughout the reaction. The precipitate was recovered by evaporation at 50 °C for 1 h. The product was dissolved in ethanol, recrystallized from diethyl ether, and dried at room temperature in vacuum. 1 mol L^{-1} $MAPbBr_3$ solution was prepared by the reaction between the as-synthesized MABr powder and $PbBr_2$ at 1:1 mol ratio in *N*,*N*-dimethylformamide (DMF).

2.2. Synthesis of $MAPbBr_3$ crystals on FTO glass substrate

Fluorine-doped tin oxide (FTO) glass substrate was cleaned by ultrasonication in deionized water, iso-propanol (IPA) and acetone twice, and subjected to microwave O_2 plasma treatment for 1.5 min. O_2 plasma treatment can effectively detach the adsorbed moieties and improve the hydrophilicity of the FTO substrate. The synthesis of $MAPbBr_3$ crystals on FTO glass substrate was conducted in a glove box. In specific, 1 mol L^{-1} $MAPbBr_3$ in DMF solution was spin-coated on FTO glass substrate at 3000 rpm for 50 s and dried on a hot plate at 100 °C for 20 min.

2.3. Synthesis of $MAPb(Br_{1-x}I_x)_3$ crystals by anion exchange on FTO glass substrate

MAI powder was synthesized according to the literature by a solution reaction [6], which consisted of 24 mL of methylamine solution (33 wt% in ethanol) and 10 mL of hydroiodic acid (HI, 57 wt%) in a 250 mL round-bottom flask under nitrogen atmosphere at 0 °C for 2 h with stirring. The precipitate was recovered by evaporation at 50 °C for 2 h, washed with diethyl ether three times, and finally dried at 60 °C in vacuum. The MAI power was dissolved in IPA to form 4 mg mL^{-1} solution. The $MAPbBr_3$ crystals on FTO glass substrate were placed into a glass bottle (volume 15 mL) filled with 5 mL of MAI solution. It was then sealed and transferred into an oven at 60 °C for the anion exchange reaction. It is worth noting that the anion exchange process was air-sensitive. So the vial was essentially sealed in inert atmosphere before transferring to an oven. After certain time, the FTO glass was taken out with the tweezers and quickly dipped into IPA to wash away attached MAI, dried by air blowing. Finally, the product on FTO glass substrate was stored in a glove box for further study.

2.4. Characterization

Powder X-ray diffraction patterns (XRD) were recorded on a Rigaku SmartLab diffraction system with high-intensity Cu Kα (λ = 0.15406 nm) radiation. Field-emission scanning electron microscope (FESEM) images were obtained on Fei Quanta 400 F operated at an accelerating voltage of 10.0 kV. UV–visible absorption spectra were carried out on a Hitachi U-3501 spectrophotometer.

2.5. Finite-difference time-domain method (FDTD) simulation

The absorption spectrum of the perovskite structure was simulated with Lumerical FDTD Solutions. The complex refractive index of $MAPbI_3$ was adopted from the supporting information of Xie's report [25]. A Gaussian source in the wavelength of 400–850 nm was used in the simulation. In the solid rectangular structure, configuration of 500 nm-thick layer of $MAPbI_3$ covered with 100-nm-thick layer of gold was adopted to mimic the real device structure. The light source illuminated from the perovskite side from the bottom. In the open-box-like structure, a 100-nm-thick of gold covered the caved side and the same light source illuminated from the perovskite side.

3. Results and discussion

Fig. 1a exhibits X-ray diffraction (XRD) patterns of the $MAPb(Br_{1-x}I_x)_3$ crystals obtained by immersing $MAPbBr_3$ crystals in MAI solution for different time. The diffraction pattern of the product before soaking (0 min) matches that of the cubic phase perovskite $MAPbBr_3$ [22]. After immersing the $MAPbBr_3$ crystals in MAI solution, all of the diffraction peaks of the products shift toward smaller angles, indicating an expanded lattice constant due to the formation of $MAPb(Br_{1-x}I_x)_3$. For easy comparison of the peak shift, the magnified diffraction peak in the 2θ range of 13.8–15.2° is presented in Fig. 1b. It can be seen that the diffraction peak at 14.90° corresponding to the (100) plane of $MAPbBr_3$ crystals is shifted to 14.76° upon immersing the $MAPbBr_3$ crystals in MAI solution for 5 min. When soaking time is increased to 15 min, the peak is further shifted to 14.63°, demonstrating the increased I content in the product. Meanwhile, there appears another peak at 14.30°, indicating the formation of a different $MAPb(Br_{1-x}I_x)_3$ phase with higher I content. As the immersing time is prolonged to 30 min, the two peaks merge into a single plateau shape centered at 14.48°, illustrating the product is still multi-component mixture of $MAPb(Br_{1-x}I_x)_3$ crystals with different Br and I ratio. For even extended immersing time, the peak is further shifted to lower 2θ degrees, at 14.29° with 60 min, 14.22° with 90 min, 14.15° with 2 h, 14.11° with 3 h and 4 h. The major diffraction peak at 14.11° can be indexed to (110) plane of tetragonal $MAPbI_3$ crystals, along with the peaks at 19.99°, 28.44°, 31.88° and 43.24° from (200), (220), (310) and (330) planes, respectively. The XRD diffraction pattern confirms that the cubic $MAPbBr_3$ are completely converted to tetragonal $MAPbI_3$ after 3 h immersion [22,26]. Therefore, the $MAPb(Br_{1-x}I_x)_3$ ($0 \leqslant x \leqslant 1$) crystals with tunable composition can be acquired by this anion

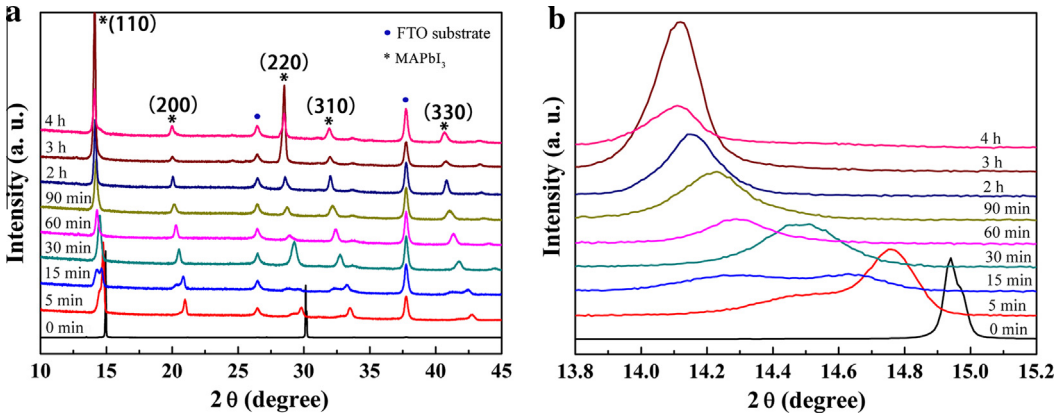

Fig. 1. X-ray diffraction patterns of as-synthesized $MAPb(Br_{1-x}I_x)_3$ products.

exchange approach, in which higher I content was obtained with prolonged soaking time.

The scanning electron microscopy (SEM) images of the products harvested at different reaction times are shown in Fig. 2 at high magnification and Fig. S1 at low magnification. It shows the original $MAPbBr_3$ microcrystals possess cuboid shape with edge ranging from 2 to 3 μm and have a tiny nick on the upper surface. The crystal growth is anticipated to start from $PbBr_2$ occurred at the spin coating stage, since $PbBr_2$ has a relatively low solubility in DMF. As the solvent evaporates during the spinning process, $PbBr_2$ quickly precipitates at the initial stage and acts as the crystallization seeds, which easily reacts with MABr in the solution even at room temperature, forming $MAPbBr_3$ due to the small activation energy. The crystal finally grows into cuboid morphology as shown in Fig. 2a. Interestingly, most of the particles have a shallow round pit in the center of the surface, which may come from the volatilization of DMF solvent. After the $MAPbBr_3$ microcrystals immersed in MAI solution for 5 min, small nanoparticles appeare on the surface of the cubes, indicating the formation of $MAPb(Br_{1-x}I_x)_3$ crystals. When the soaking time is extended to 15 min, more nanoparticles are formed on the cubic surface and the void in the upper surface became more obvious. With further prolonged soaking time of 30 min, the products show open-box-like morphologies while maintaining the initial $MAPbBr_3$ cuboid framework. Afterward, the basic framework is still kept with prolonged soaking time up to 4 h, while no obvious dissolution of the as-formed perovskite is observed. Therefore, $MAPb(Br_{1-x}I_x)_3$ crystals ($0 \leqslant x \leqslant 1$) with targeted geometric characteristics are obtained, in which the overall crystal shapes are dependent on the morphology of original $MAPbBr_3$ crystals. Meanwhile, the partial dissolution of the crystals in the center of the surface leaves voids in the crystals. In addition, the conversion rate of the process can be adjusted by the concentration of MAI and the temperature, which is decreased when the concentration of MAI is halved, with the complete conversion of $MAPbBr_3$ to $MAPbI_3$ after 8 h; while accelerated as MAI concentration doubled, requiring about 2 h for complete conversion. The final morphologies of the products are similar to that of the 4 mg mL^{-1} MAI solution (Fig. S2a and b). These results disclose a general trend: the greater the concentration of MAI, the more rapid conversion of $MAPbBr_3$ to $MAPbI_3$ crystals. When the reaction carried out at room temperature, the exchange of bromide by iodide becomes very slow and incomplete even for 24 h (SEM image shown in Fig. S2c), demonstrating that it lacks thermodynamic driving force for the significant lattice expansion associated with the substitution of Br^- by I^- at room temperature, which is consistent with Grätzel's report in which bromide in $MAPbBr_3$ crystals is only partially replaced by iodide at room temperature [27]. If the FTO glass substrate is preliminarily spin-coated with a dense TiO_2 blocking layer (bl-TiO_2) of ca. 50 nm thickness, the morphology and coverage of $MAPbBr_3$ microcrystals are basically unchanged and the subsequent anion exchange are also similar to that synthesized by direct spin-coating on FTO glass substrate. Therefore, the formation of cuboid $MAPbBr_3$, subsequent anion exchange and dissolution process are irrelevant to substrates, indicating the adaptability of the synthetic method.

The structure of lead halide perovskite $MAPbX_3$ (X = Cl, Br or I) is a 3D network formed by PbX_6 octahedrons connecting with each other in a corner sharing way and the methyl ammonium group MA^+ filling in the voids between the PbX_6 octahedrons. $MAPbBr_3$ has a cubic perovskite structure of the Pm $\bar{3}$ m space group at room temperature, while $MAPbI_3$ has a distorted three-dimensional perovskite structure that crystallizes in the tetragonal I4/mcm space group. The structural difference between the two perovskites originates from the differences in the ionic radius of I^- and Br^- ions with 6-fold coordination, which are 2.2 and 1.96 Å, respectively. The ionic radii relationship between M, A, and X in $MAPbX_3$ perovskite structure has been widely accepted as a criterion for the distortion of the PbX_6 octahedron; that is, the smaller X ion radius is relatively profitable for the formation and stabilization of cubic perovskite structure. When $MAPbBr_3$ crystals are dipped into MAI solution at elevated temperature, it dynamically favors the large lattice expansion associated with the substitution of Br^- by I^-, accompanied by the slight rotation of the PbX_6 octahedrons along the ⟨001⟩ axis on the (00l) plane of the ideal cubic $MAPbBr_3$ perovskite structure while maintaining their corner-sharing connectivity, as illustrated in Scheme 1a. The whole exchange process of the crystals was illustrated in Scheme 1b. Firstly, the surface of $MAPbBr_3$ crystal is covered with a layer of $MAPb(Br_{1-x}I_x)_3$ through the fast anion exchange process. It is known that the halide ion in the perovskite structure is prone to moving within the lattice [28]. A fast anion exchange process of Br^- by I^- is anticipated to happen due to the concentration of iodide ion being higher than the bromide ion in the surrounding environment, resulting in a layer of $MAPb(Br_{1-x}I_x)_3$ crystals covering on the $MAPbBr_3$ crystal. This layer of iodine-rich phase $MAPb(Br_{1-x}I_x)_3$ will retard the $MAPbBr_3$ crystal dissolution from the surface into the DMF solution. The inner part of $MAPbBr_3$ crystal begins to dissolve attacked by the IPA solvent, which firstly decomposes to MABr and $PbBr_2$, then further formed Br_3^- by Br^- from MABr with $PbBr_2$ [29]. Thus, voids form in the middle of the crystal, resulting in open-box-like $MAPb(Br_{1-x}I_x)_3$ crystals. Herein, the void formation in the crystal comes from the internal dissolution of the crystal, which can be attributed to Kerkindall effect. Finally, an open-box-like structure of $MAPbI_3$ crystal is formed by the full conversion of $MAPbBr_3$

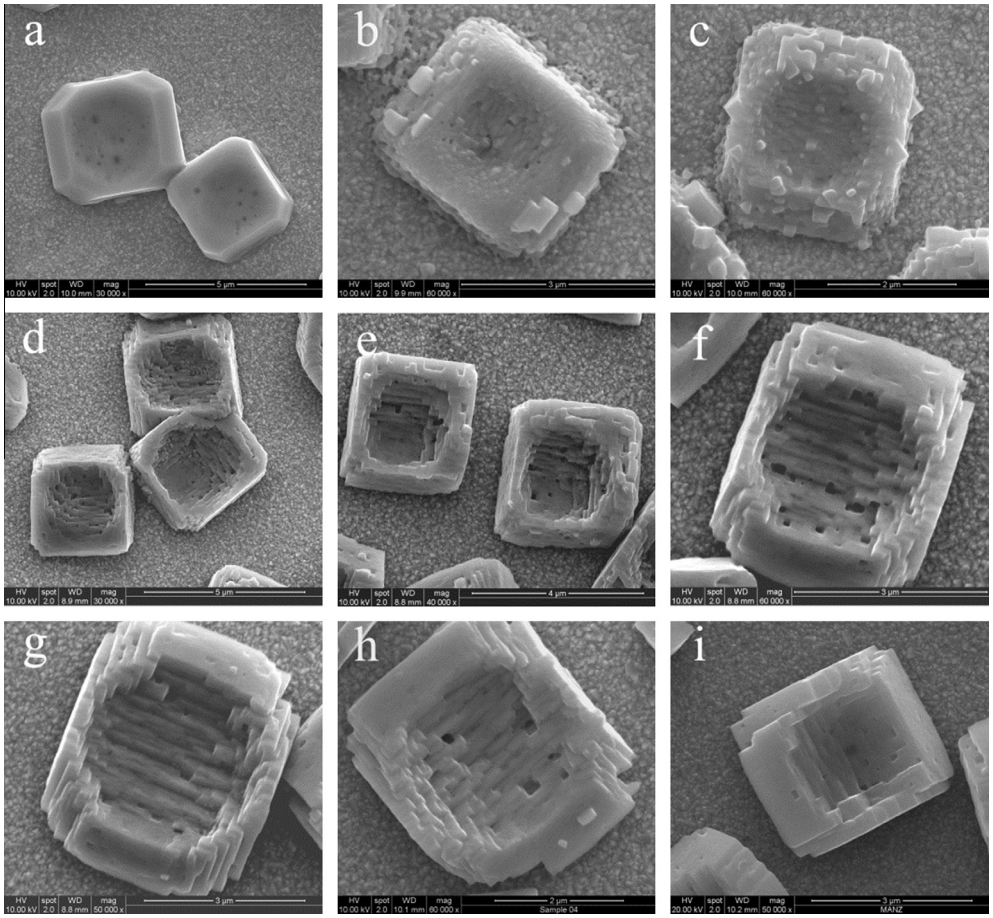

Fig. 2. SEM images of the $MAPb(Br_{1-x}I_x)_3$ microcrystals synthesized by soaking $MAPbBr_3$ microcrystals in MAI solution at 60 °C with different time. (a) 0 min. (b) 5 min. (c) 15 min. (d) 30 min. (e) 60 min. (f) 90 min. (g) 2 h. (h) 3 h. (i) 4 h.

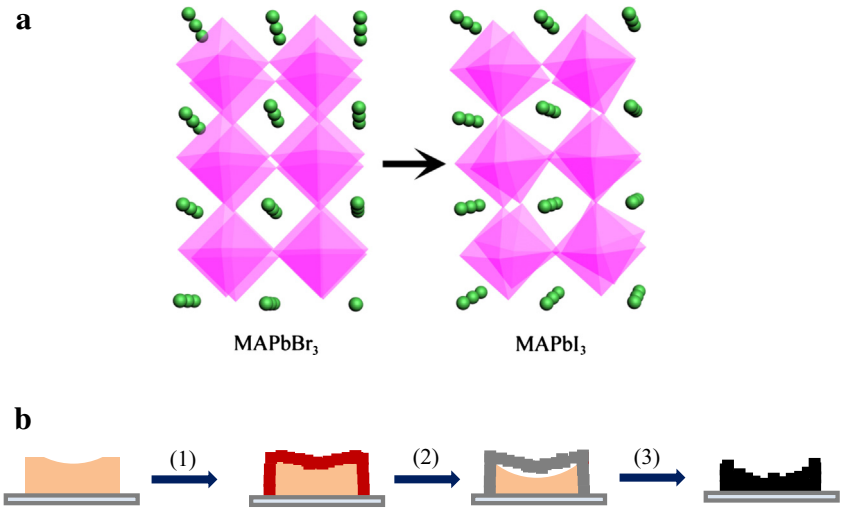

Scheme 1. (a) Schematic illustrating the crystal structure change upon the transformation from $MAPbBr_3$ to $MAPbI_3$ crystals. The data are from Ref. [29]. (b) The proposed mechanism for the conversion from $MAPbBr_3$ microcrystals to open-box-like $MAPbI_3$ microcrystals.

through the anion exchange and internal dissolution process. Afterwards, a dynamic equilibrium state is established, where the morphology of the crystal changes little due to the equivalent dissolution and recrystallization rate.

Because $MAPbI_3$ has a distorted three-dimensional perovskite structure, the tetragonal phase of $MAPb(Br_{1-x}I_x)_3$ crystals can be defined as a pseudocubic (pc) lattice, and the (100)pc spacing in a pseudocubic crystal system can match its (110)t spacing in a

Table 1
The lattice parameter, I atom content, the onset absorption band and band gap of $MAPb(Br_{1-x}I_x)_3$ crystals with different soaking time.

Time (min)	a (Å)	x	λ (nm)	E_g (eV)
0	5.925	0	533	2.33
5	5.997	0.18	586	2.12
15	6.050	0.32	625	1.99
30	6.120	0.47	672	1.85
60	6.193	0.68	725	1.71
90	6.219	0.74	749	1.66
120	6.254	0.83	775	1.60
180	6.267	1	784	1.58
240	6.272	1	784	1.58

Note: The product soaked with 15 min was calculated with the peak at 14.63°. The band gap is estimated from the onset absorption band.

tetragonal (t) crystal system. The replacement of Br^- by I^- ions in $MAPbBr_3$ crystals causes the systematic shift of (100)c peak toward lower 2θ degrees because the gradual substitution increases the lattice spacing. The lattice parameter of the $MAPb(Br_{1-x}I_x)_3$ phases can be indexed by pseudocubic or cubic phase as a function of Br content [30]. The lattice parameter and I atom content of the $MAPb(Br_{1-x}I_x)_3$ product are listed in Table 1, which indicate that the I/Br ratio can be tuned in the entire range ($0 \leqslant x \leqslant 1$) by the simple anion exchange process.

The UV–visible absorption spectra of $MAPb(Br_{1-x}I_x)_3$ ($0 \leqslant x \leqslant 1$) were measured to study the variation of optical properties in the hybrid perovskite, as shown in Fig. 3a. The onset absorption band of $MAPb(Br_{1-x}I_x)_3$ hybrids can be tuned from 533 nm (2.33 eV) to 784 nm (1.58 eV) (Table 1). Fig. 3b shows the corresponding colors of $MAPb(Br_{1-x}I_x)_3$ on FTO glass substrate ($0 \leqslant x \leqslant 1$). Through the compositional control of $MAPb(Br_{1-x}I_x)_3$, the color could be tuned from yellow for $MAPbBr_3$ ($x = 0$) to brown for $MAPb(Br_{1-x}I_x)_3$ ($0 < x < 1$) and black for $MAPbI_3$ ($x = 1$). Since the perovskite microcrystals are discontinuously distributed on the substrates, the films display semi-transparent characteristics, allowing for the fabrication of colorful and semi-transparent devices. A systematic shift of the absorption band edge to longer wavelength with increasing

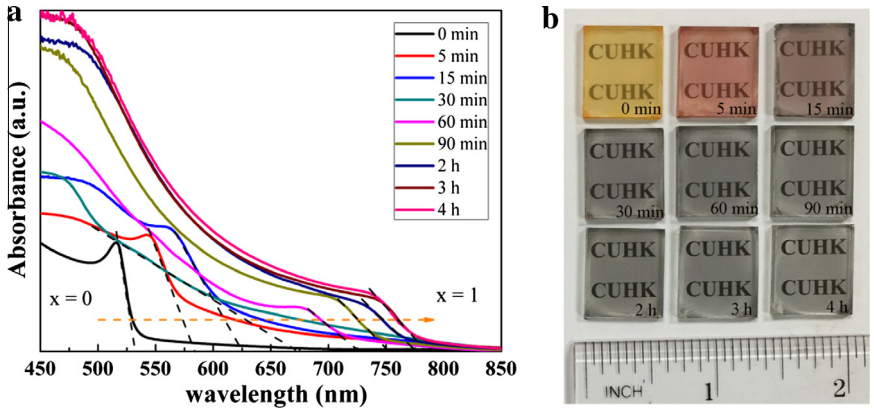

Fig. 3. UV–vis absorption spectra and photographs of the as-synthesized $MAPb(Br_{1-x}I_x)_3$ products. (a) UV–vis absorption spectra of $MAPb(Br_{1-x}I_x)_3$ on FTO substrate. (b) Photographs of $MAPb(Br_{1-x}I_x)_3$ on FTO substrate.

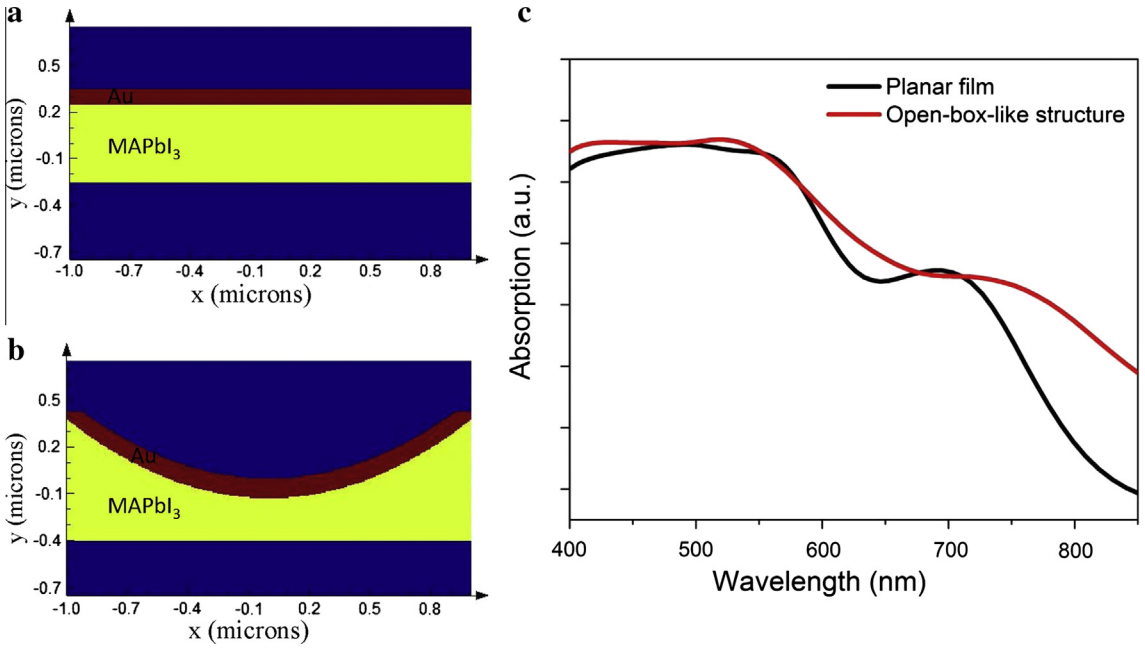

Fig. 4. FDTD simulated absorption of $MAPbI_3$. (a) Solid rectangular structure and (b) open-box-like structure of $MAPbI_3$ coupled with 100-nm-thick gold. (c) The absorption spectrum of solid rectangular and open-box-like structures.

I content in MAPb($Br_{1-x}I_x$)$_3$ indicates that the energy band gap (E_g) can be tuned by altering the elemental composition of the hybrid perovskite, as shown in Table 1.

In order to gain further insight into the optical properties of the perovskite material, we simulate the absorption properties of the open-box-like perovskite structure and a solid rectangular configuration (Fig. 4). We take $MAPbI_3$ as the simulated material. To fully mimic the device structure in conventional perovskite solar cells, we introduce an Au film with thickness of 100 nm on the surface of the perovskite nanostructures. It is found that the light absorption of the caved structure is considerably enhanced in the near infrared region when compared with that of the rectangular structure (Fig. 4c). According to the light absorption spectrum of $MAPbI_3$, the perovskite show relatively low absorption coefficient in the longer wavelength. In this regard, the caved structure is an excellent candidate for the improvement of the overall light harvesting efficiency. Because the surface coverage of the caved structure is quite low, we do not examine it in real device at this moment. In the future study, we will try to make higher density of distribution of the caved perovskite for solar cell investigation.

4. Conclusions

In summary, the band gap tunable open-box-like MAPb($Br_{1-x}I_x$)$_3$ ($0 \leqslant x \leqslant 1$) microcrystals are obtained through anion exchange by soaking $MAPbBr_3$ cubic microcrystals in MAI solution. The framework of $MAPbBr_3$ crystals is basically remained in the final MAPb($Br_{1-x}I_x$)$_3$ crystals by *in situ* substitution of Br^- ions with I^- ions. Meanwhile, the faster dissolution of the inner part of the $MAPbBr_3$ than the outer surface leaves voids in the center of the crystals, forming open-box-like MAPb($Br_{1-x}I_x$)$_3$ crystals. The optical absorption of the product caused by band gap engineering can be controllably tuned to cover almost the entire visible spectrum. From different initial morphologies of $MAPbX_3$, a variety of microstructures are anticipated to be obtained through this anion exchange and internal dissociation process with controllable halide composition, therefore, expanding the platform to exploit the properties and application of organic lead halide perovskites.

Acknowledgements

This work was financially supported by the Natural Science Foundation of China (21201007) and Theme-based Research Scheme (Project No. T23-407/13-N) from the Research Grants Council of the Hong Kong Special Administrative Region, China.

Appendix A. Supplementary material

Supplementary data associated with this article can be found, in the online version, at http://dx.doi.org/10.1016/j.jcis.2015.09.005.

References

[1] J. Burschka, N. Pellet, S.-J. Moon, R. Humphry-Baker, P. Gao, M.K. Nazeeruddin, M. Grätzel, Nature 499 (2013) 316–319.
[2] M. Liu, M.B. Johnston, H.J. Snaith, Nature 501 (2013) 395–398.
[3] A. Kojima, K. Teshima, Y. Shirai, T. Miyasaka, J. Am. Chem. Soc. 131 (2009) 6050–6051.
[4] N.J. Jeon, H.G. Lee, Y.C. Kim, J. Seo, J.H. Noh, J. Lee, S.I. Seok, J. Am. Chem. Soc. 136 (2014) 7837–7840.
[5] G. Xing, N. Mathews, S. Sun, S.S. Lim, Y.M. Lam, M. Grätzel, S. Mhaisalkar, T.C. Sum, Science 342 (2013) 344–347.
[6] S.D. Stranks, G.E. Eperon, G. Grancini, C. Menelaou, M.J. Alcocer, T. Leijtens, L.M. Herz, A. Petrozza, H.J. Snaith, Science 342 (2013) 341–344.
[7] N.J. Jeon, J.H. Noh, W.S. Yang, Y.C. Kim, S. Ryu, J. Seo, S.I. Seok, Nature 517 (2015) 476–480.
[8] P. You, Z. Liu, Q. Tai, S. Liu, F. Yan, Adv. Mater. (2015), http://dx.doi.org/10.1002/adma.201501145.
[9] G.E. Eperon, V.M. Burlakov, P. Docampo, A. Goriely, H.J. Snaith, Adv. Funct. Mater. 24 (2014) 151–157.
[10] P. Docampo, J.M. Ball, M. Darwich, G.E. Eperon, H.J. Snaith, Nat. Commun. 4 (2013) 2761.
[11] J.H. Heo, S.H. Im, J.H. Noh, T.N. Mandal, C.-S. Lim, J.A. Chang, Y.H. Lee, H.-J. Kim, A. Sarkar, Md.K. Nazeeruddin, M. Gratzel, S.I. Seok, Nat. Photonics 7 (2013) 487–492.
[12] B. Conings, L. Baeten, C. De Dobbelaere, J. D'Haen, J. Manca, H.-G. Boyen, Adv. Mater. 26 (2014) 2041–2046.
[13] J.H. Heo, D.H. Song, S.H. Im, Adv. Mater. 26 (2014) 8179–8183.
[14] J.H. Im, C.R. Lee, J.W. Lee, S.W. Park, N.G. Park, Nanoscale 3 (2011) 4088–4093.
[15] K. Liang, D.B. Mitzi, M.T. Prikas, Chem. Mater. 10 (1998) 403–411.
[16] Q. Chen, H.P. Zhou, Z.R. Hong, S. Luo, H.-S. Duan, H.-H. Wang, Y.S. Liu, G. Li, Y. Yang, J. Am. Chem. Soc. 136 (2014) 622–625.
[17] B.E. Cohen, S. Gamliel, L. Etgar, APL Mater. 2 (2014) 081502.
[18] S. Yang, Y.C. Zheng, Y. Hou, X. Chen, Y. Chen, Y. Wang, H. Zhao, H.G. Yang, Chem. Mater. 26 (2014) 6705–6710.
[19] S.T. Ha, X. Liu, Q. Zhang, D. Giovanni, T.C. Sum, Q. Xiong, Adv. Opt. Mater. 2 (2014) 838–844.
[20] Q. Zhang, S.T. Ha, X.F. Liu, T.C. Sum, Q.H. Xiong, Nano Lett. 14 (2014) 5995–6001.
[21] H.M. Zhu, Y.P. Fu, F. Meng, X.X. Wu, Z.Z. Gong, Q. Ding, M.V. Gustafsson1, M.T. Trinh, S. Jin, X.Y. Zhu, Nat. Mater. 14 (2015). 636–U115.
[22] Y.P. Fu, F. Meng, M.B. Rowley, B.J. Thompson, M.J. Shearer, D.W. Ma, R.J. Hamers, J.C. Wright, S. Jin, J. Am. Chem. Soc. 137 (2015) 5810–5818.
[23] S.F. Zhuo, J.F. Zhang, Y.M. Shi, Y. Huang, B. Zhang, Angew. Chem. Int. Ed. 54 (2015) 5693–5696.
[24] T. Kollek, D. Gruber, J. Gehring, E. Zimmermann, L. Schmidt-Mende, S. Polarz, Angew. Chem. Int. Ed. 54 (2015) 1341–1346.
[25] F.X. Xie, D. Zhang, H.M. Su, X.G. Ren, K.S. Wong, M. Grätzel, W.C.H. Choy, ACS Nano 9 (2015) 639–646.
[26] T. Baikie, Y. Fang, J.M. Kadro, M. Schreyer, F. Wei, S.G. Mhaisalkar, M. Graetzel, T.J. White, J. Mater. Chem. A 1 (2013) 5628–5641.
[27] N. Pellet, J. Teuscher, J. Maier, M. Grätzel, Chem. Mater. 27 (2015) 2181–2188.
[28] A. Dualeh, T. Moehl, N. Tétreault, J. Teuscher, P. Gao, M.K. Nazeeruddin, M. Grätzel, ACS Nano 8 (2014) 362–373.
[29] T.X. Wang, M.D. Kelley, J.N. Cooper, R.C. Beckwith, D.W. Margerum, Inorg. Chem. 33 (1994) 5872–5878.
[30] J.H. Noh, S.H. Im, J.H. Heo, T.N. Mandal, S.I. Seok, Nano Lett. 13 (2013) 1764–1769.